



Design of mesostructured $\text{H}_3\text{PW}_{12}\text{O}_{40}$ -titania materials with controllable structural orderings and pore geometries and their simulated sunlight photocatalytic activity towards diethyl phthalate degradation

Kexin Li^{a,b}, Xia Yang^a, Yingna Guo^a, Fengyan Ma^a, Huichao Li^a, Ling Chen^a, Yihang Guo^{a,*}

^a School of Chemistry, Northeast Normal University, Changchun 130024, PR China

^b School of Environmental and Chemical Engineering, Nanchang Hangkong University, Nanchang 330063, PR China

ARTICLE INFO

Article history:

Received 17 April 2010

Received in revised form 11 July 2010

Accepted 13 July 2010

Available online 21 July 2010

Keywords:

Mesoporous material

Polyoxometalate

Titania

Simulated sunlight photocatalysis

Endocrine disrupting chemical

ABSTRACT

A series of mesostructured $\text{H}_3\text{PW}_{12}\text{O}_{40}$ -titania materials with two-dimensional hexagonal, three-dimensional cubic, and three-dimensional interconnected sponge-like pore geometries were developed by using a single step nonionic-surfactant-templating strategy combined with evaporation-induced self-assembly (EISA) or hydrothermal treatment technique. The mesostructure, morphology, porosity, optical absorption property as well as composition and structure of as-prepared materials were well-characterized. Subsequently, the materials were successfully applied to the degradation of an aqueous diethyl phthalate (a kind of endocrine disrupting chemical) under the simulated sunlight irradiation at $\lambda > 320$ nm and $\lambda > 400$ nm region, respectively, and special attention was paid to investigate the influences of the structural orderings, pore geometries, $\text{H}_3\text{PW}_{12}\text{O}_{40}$ loadings as well as calcination temperature on the photocatalytic performance of the $\text{H}_3\text{PW}_{12}\text{O}_{40}$ -titania materials to the target reaction.

© 2010 Elsevier B.V. All rights reserved.

1. Introduction

The development of efficient TiO_2 -based photocatalytic materials still offers unexplored opportunities for total destruction of hazardous organic compounds in polluted air/water with the aid of solar light, owing to their environmental-friendly benefits in the saving of resources [1,2]. Semiconductor TiO_2 has consistently drawn much attention for their fascinating potential in environmental applications [3–5]. However, as a wide band gap semiconductor (3.2 eV), TiO_2 can only absorb UV fraction of solar light (3–5%), which leads to solar light-assisted TiO_2 photocatalytic process performs in very low efficiency [6]; on the other hand, quantum efficiency of TiO_2 is low due to fast recombination of photoinduced electron–hole ($\text{h}^+ - \text{e}^-$) pairs [7,8]. To overcome the above two drawbacks, extensive research endeavors, therefore, have been devoted to design novel TiO_2 -based photocatalysts with high photocatalytic efficiency, by extending the light-response range of TiO_2 to visible-light region and/or by reducing the $\text{h}^+ - \text{e}^-$ recombination probability. To realize this aim, numerous research attempts are currently being employed including crystal growth to tailor phase, shape, defect, and size of TiO_2 together with its crystallinity [9,10]; metal or non-metal doping to modify electronic structure [11–14]; and heterostructuring design of integrated multi-semiconductor

systems to promote the separation of $\text{h}^+ - \text{e}^-$ pairs and/or modify electronic structure [15–17].

Additionally, the performance of the heterogeneous photocatalysts is also determined to a great extent by their textural and morphological properties, and fabrication of solid photocatalysts with perfect porous structure including uniform pore channel, large surface area, and larger pore diameter can improve their photocatalytic activity by increase active site numbers and the accessibility of active sites to the substrate [18]. Porous materials, especially mesoporous materials with unique surface physico-chemical properties, have been successfully applied in many liquid phase catalytic processes [19–21]. Relying on sol–gel, solution, and surface chemistry, there is great potential to explore novel strategies for mesoporous catalytic materials with controllable wall components and the morphological architectures [22,23].

For the purpose of the improvement of the overall efficiency of TiO_2 -based photocatalytic process, herein we developed a series of mesostructured $\text{H}_3\text{PW}_{12}\text{O}_{40}$ -titania materials with different textural and morphological properties. $\text{H}_3\text{PW}_{12}\text{O}_{40}$ (12-tungstophosphoric acid), a kind of widely used polyoxometalate (POM) in homogeneous acid- and photocatalytic reactions, is a very strong Brønsted acid and efficient electron trap with well-defined Keggin structure [24–29]. $\text{H}_3\text{PW}_{12}\text{O}_{40}$ shares very similar photochemical characteristics of the semiconductor photocatalysts due to their similar electronic attributes. Several group's research has proved the combination of the $\text{H}_3\text{PW}_{12}\text{O}_{40}$ with TiO_2 can enhance the photocatalytic efficiency of TiO_2 -

* Corresponding author. Tel.: +86 431 85098705; fax: +86 431 85098705.
E-mail address: guoyh@nenu.edu.cn (Y. Guo).

catalyzed reaction due to the strong electron accept ability of POM and the transfer of electrons from $\text{H}_3\text{PW}_{12}\text{O}_{40}$ to oxygen species present in the reaction medium [30,31]. Our previous studies also found this synergistic photocatalytic effect between POM and TiO_2 . POM/ TiO_2 materials (POM = $\text{H}_3\text{PW}_{12}\text{O}_{40}$ or $\text{H}_6\text{P}_2\text{W}_{18}\text{O}_{62}$) prepared by a sol–gel co-condensation method exhibited higher photocatalytic activity under both UV ($\lambda > 254\text{ nm}$) and visible-light ($\lambda > 400\text{ nm}$) irradiation towards dye degradation compared with bare TiO_2 [32,33]. More recently, Marci's group reported that the photocatalytic degradation of 2-propanol under solar simulating Xe lamp irradiation ($\lambda > 320\text{ nm}$) occurred successfully by using $\text{H}_3\text{PW}_{12}\text{O}_{40}$ –titania material prepared by a post-synthesized method [34]. However, both of the above preparation strategies need to be ameliorated: for the $\text{H}_3\text{PW}_{12}\text{O}_{40}/\text{TiO}_2$ materials obtained by a co-condensation method in the absence of any structure-directing agent, its mesostructure was formed due to aggregation among product particles, resulting in the mesophase with uneven pore diameter distribution; in the case of $\text{H}_3\text{PW}_{12}\text{O}_{40}$ –titania materials prepared by a post-synthesized method, it suffered from the problems such as the Keggin unit leaching, poor control over $\text{H}_3\text{PW}_{12}\text{O}_{40}$ loading, small specific surface area, and aggregation of the Keggin unit at the composite surface [35–37]. All of these lead to reduced photocatalytic activity of the supported POMs.

In search for new routes to prepare $\text{H}_3\text{PW}_{12}\text{O}_{40}$ –titania materials with excellent photocatalytic behaviors, nonionic-surfactant-templating strategy combined with evaporation-induced self-assembly (EISA) or hydrothermal treatment technique were applied in current work. These two strategies can lead to the $\text{H}_3\text{PW}_{12}\text{O}_{40}$ –titania materials with different textural and morphological properties, optical absorption properties, crystallinity, and the surface states. All of these factors can affect the photocatalytic activity of as-prepared $\text{H}_3\text{PW}_{12}\text{O}_{40}$ –titania materials. Additionally, by using this one-pot preparation process, the interaction between the Keggin unit and TiO_2 matrix is strong, which can avoid the drop of the Keggin unit from the matrix during the preparation and subsequent photocatalytic process.

The photocatalytic activity of as-prepared $\text{H}_3\text{PW}_{12}\text{O}_{40}$ –titania ($\text{H}_3\text{PW}_{12}\text{O}_{40}/\text{TiO}_2$) was evaluated in terms of the degradation and mineralization of diethyl phthalate (DEP) under solar simulating Xe lamp irradiation in the near UV- ($\lambda > 320\text{ nm}$) and visible-light ($\lambda > 400\text{ nm}$) region, respectively. DEP is a member of phthalate ester (PAE) family, while PAEs are endocrine disrupting chemicals that have a wide variety of industrial, agricultural, and domestic application, especially for their uses as plasticizers. The release of PAEs into the ecosystem or wastewater effluent has caused many human diseases and pollution. PAEs are rather stable compounds in the natural environment, and they recalcitrant to biodegradation and photolytic degradation owing to the existence of benzene carboxylic group and the lack of light response at wavelengths longer than 300 nm [38]. Therefore, it is urgent to search for alternative and effective treatment processes for such pollutants. In addition, unlike dyes that possess light response in the visible-light area, degradation of DEP due to the sensitization effect can be excluded in current photocatalytic system. During the $\text{H}_3\text{PW}_{12}\text{O}_{40}/\text{TiO}_2$ -catalyzed DEP degradation process, the influences of $\text{H}_3\text{PW}_{12}\text{O}_{40}$ loadings, mesostructural orderings and pore geometries as well as calcination temperature on the photocatalytic performance were also studied.

2. Experimental

2.1. Chemicals and reagents

Titanium tetraisopropoxide ($\text{Ti}(\text{Oi-Pr})_4$, abbreviated TTIP, 98.0%), 12-tungstophosphoric acid ($\text{H}_3\text{PW}_{12}\text{O}_{40}$, 99.9%), P123

($\text{EO}_{20}\text{PO}_{70}\text{EO}_{20}$, where $\text{EO} = -\text{CH}_2\text{CH}_2\text{O}-$, $\text{PO} = -\text{CH}_2(\text{CH}_3)\text{CHO}-$), and F127 ($\text{EO}_{106}\text{PO}_{70}\text{EO}_{106}$) were purchased from Aldrich. Titanium tetrachloride (99.0%) and diethyl phthalate ($\text{C}_{12}\text{H}_{14}\text{O}_4$, GC grade) were purchased from Tianjin Guangfu Fine Chemical Research Institute. All chemicals were used without further purification. The double distilled water was used throughout the catalyst preparation and subsequent catalytic test.

2.2. Preparation of mesostructured $\text{H}_3\text{PW}_{12}\text{O}_{40}/\text{TiO}_2$ materials with controllable structural orderings and pore geometries

2.2.1. Ordered 2D and 3D $\text{H}_3\text{PW}_{12}\text{O}_{40}/\text{TiO}_2$ materials

P123 (1.5 g) was dissolved with ethanol (6 mL) at room temperature. A $\text{TiCl}_4/\text{TTIP}$ solution was prepared by dropping TiCl_4 (1.4 mL) and TTIP (2.25 mL) into ethanol (6 mL) under vigorous stirring for 10 min. The desired amount of $\text{H}_3\text{PW}_{12}\text{O}_{40}$ (0.06, 0.12, 0.18, 0.30, and 0.48 mmol) was dissolved in water (5.2 mL). The $\text{TiCl}_4/\text{TTIP}$ ethanol solution and the $\text{H}_3\text{PW}_{12}\text{O}_{40}$ aqueous solution were successively added in the above P123 ethanol solution. After stirring the resulting mixture for 2 h at room temperature, a semi-transparent sol was obtained. The sol was transferred into a Petri dish and aged at 40°C until a uniform thin layer was formed. After being strengthened at 120°C for 24 h, the obtained powder was extracted by ethanol at 60°C for 3 h to remove P123 template (the procedure was repeated twice). Finally, the product was dried at 60°C for 24 h and crystallized at 350°C for 1 h. The product was denoted as $\text{H}_3\text{PW}_{12}\text{O}_{40}/\text{TiO}_2\text{-}2\text{D}_{\text{hex-x}}$, where x represents $\text{H}_3\text{PW}_{12}\text{O}_{40}$ loading in the composite material. For comparison, $\text{TiO}_2\text{-}2\text{D}_{\text{hex}}$ and $\text{H}_3\text{PW}_{12}\text{O}_{40}/\text{TiO}_2\text{-x}$ (without template) samples were prepared in the absence of $\text{H}_3\text{PW}_{12}\text{O}_{40}$ and template, respectively; $\text{H}_3\text{PW}_{12}\text{O}_{40}/\text{TiO}_2\text{-}2\text{D}_{\text{hex-x}}$ (400°C) and $\text{H}_3\text{PW}_{12}\text{O}_{40}/\text{TiO}_2\text{-}2\text{D}_{\text{hex-x}}$ (450°C) materials were prepared under the crystallization temperature at 400°C and 450°C , respectively.

The preparation route of ordered 3D $\text{H}_3\text{PW}_{12}\text{O}_{40}/\text{TiO}_2\text{-}3\text{D}_{\text{cub}}$ materials is similar to that of the $\text{H}_3\text{PW}_{12}\text{O}_{40}/\text{TiO}_2\text{-}2\text{D}_{\text{hex}}$ materials by using F127 instead of P123 as a template. Additionally, temperature for the stirring the mixture of $\text{TiCl}_4/\text{TTIP}$, F127, and $\text{H}_3\text{PW}_{12}\text{O}_{40}$ was set at 40°C rather than room temperature.

2.2.2. 3D sponge-like $\text{H}_3\text{PW}_{12}\text{O}_{40}/\text{TiO}_2$ materials

P123 (1.5 g) was dissolved in ethanol (6 mL) at room temperature. A $\text{TiCl}_4/\text{TTIP}$ solution was prepared by dropping TiCl_4 (1.4 mL) and TTIP (2.25 mL) into ethanol (6 mL) under vigorous stirring for 10 min. $\text{H}_3\text{PW}_{12}\text{O}_{40}$ (0.12 mmol) was dissolved in water (5.2 mL). The above $\text{TiCl}_4/\text{TTIP}$ ethanol solution and aqueous $\text{H}_3\text{PW}_{12}\text{O}_{40}$ solution was successively added into the P123/ethanol solution. After stirring the resulting mixture for 2 h at room temperature, a semi-transparent sol was obtained. The sol was subjected to hydrothermal treatment at 150°C for 48 h at a heat rate of $2^\circ\text{C}/\text{min}$. The resulting white hydrogel was dehydrated at 60°C for 24 h until complete gel particulate was formed. After thermal treatment at 120°C for 24 h, the obtained powder was extracted by ethanol at 60°C for 3 h to remove template (the procedure was repeated twice). The product was denoted as $\text{H}_3\text{PW}_{12}\text{O}_{40}/\text{TiO}_2\text{-}3\text{D}_{\text{spon-1}}$.

The preparation route of $\text{H}_3\text{PW}_{12}\text{O}_{40}/\text{TiO}_2\text{-}3\text{D}_{\text{spon-2}}$ is the same as that of the $\text{H}_3\text{PW}_{12}\text{O}_{40}/\text{TiO}_2\text{-}3\text{D}_{\text{spon-1}}$ except using F127 instead of P123 as a template agent. Additionally, temperature for the stirring the mixture of $\text{TiCl}_4/\text{TTIP}$, F127, and $\text{H}_3\text{PW}_{12}\text{O}_{40}$ was set at 40°C rather than room temperature.

2.3. Characterization

Small angle X-ray scattering (SAXS) and wide angle X-ray diffraction (WXR) patterns were obtained on a D/max-2200 VPC diffractometer using $\text{Cu K}\alpha$ radiation. Transmission electron microscope (TEM), high resolution transmission electron microscope

(HRTEM), and selected area electron diffraction (SAED) micrographs were recorded on a JEM-2100F high resolution transmission electron microscope at an accelerating voltage of 200 kV. Nitrogen porosimetry measurement was performed on a Micromeritics ASAP 2020M surface area and porosity analyzer after the samples were outgassed under vacuum at 90 °C for 1 h and 200 °C for 6 h. UV–Vis diffuse reflectance spectra (UV–Vis/DRS) were recorded on a Cary 500 UV–Vis–NIR spectrophotometer. Raman scattering spectra were recorded on a Jobin-Yvon HR 800 instrument with an Ar⁺ laser source of 488 nm wavelength in a macroscopic configuration. The ³¹P MAS (magic-angle spinning) NMR spectrum was recorded on a Bruker AVANCE III 400 WB spectrometer equipped with a 4 mm standard bore CPMAS probehead whose X channel was tuned to 162 MHz for ³¹P, using a magnetic field of 9.39T at 297 K. The dried and finely powdered sample was packed in the ZrO₂ rotor closed with Kel-F cap which was spun at 12 kHz rate. The experiments were conducted at a contact time of 2 ms. A total of 128 scans were recorded with 5 s recycle delay for each sample. The ³¹P MAS chemical shifts were referenced to the resonances of monoammonium phosphate (NH₄H₂PO₄) standard ($\delta = 0.00$). FT-IR spectra were recorded on a Nicolet Magna 560 IR spectrophotometer. H₃PW₁₂O₄₀ loading in the composite material was determined by a Leeman Prodigy Spec inductively coupled plasma atomic emission spectrometer (ICP-AES).

2.4. Adsorption and photocatalytic degradation of DEP

Adsorption and photocatalytic degradation of DEP experiments of as-prepared H₃PW₁₂O₄₀/TiO₂ materials were performed in a self-made quartz photoreactor placed about 15 cm under the light source. The diameter of the reactor is 63 mm, consistent with that of facula of the light resource. For all adsorption and photocatalysis experiment, 100 mL of aqueous DEP solution with the initial concentration of 13.5 mg L⁻¹ and 150 mg of catalyst were used. The adsorption–desorption equilibrium between DEP molecules and catalyst surface was determined by measuring the DEP concentration during 60 min without light irradiation. After the adsorption–desorption equilibrium was established, the suspension including aqueous DEP and catalyst powder was irradiated by a PLS-SXE300 Xe lamp (300 W, Beijing Trusttech Co. Ltd., China) with an average light intensity of 5 mW cm⁻². The near UV-light irradiation was generated using this lamp that can simulate the solar spectrum with wavelength higher than 320 nm. The visible-light irradiation can be obtained by removing the UV irradiation from the lamp using a 400 nm cut filter. The temperature of the suspension was at 35 ± 2 °C, and the system was communicated with air. At given intervals of irradiation, fixed amounts of reaction solution were taken out, centrifuged and filtrated, and the filtrates were analyzed. Changes of the concentrations of DEP were analyzed by a Shimadzu LC-20A high pressure liquid chromatography (HPLC): C₁₈ column, UV detector ($\lambda = 227$ nm), and acetonitrile/water (80/20 v/v) was used as a mobile phase at a flow rate of 0.9 mL/min; while total organic carbon (TOC) was monitored by a Shimadzu TOC-500 Total Organic Carbon analysis system.

3. Results and discussion

3.1. Preparation of mesostructured H₃PW₁₂O₄₀/TiO₂ materials with controllable structural orderings and pore geometries

TEM combined with SAXS results indicate that as-prepared nonionic-surfactant-templated H₃PW₁₂O₄₀/TiO₂ materials with controllable structural orderings and pore geometries were obtained by using different preparation routes, i.e., EISA and

hydrothermal treatment (see Figs. 1 and 2). At the beginning of stirring the mixture of surfactant (P123 or F127) and precursors (TTIP/TiCl₄ and H₃PW₁₂O₄₀) in an ethanol/water medium at room temperature (P123-templated system) or 40 °C (F127-templated system), H₃PW₁₂O₄₀/Ti(Oi-Pr)_{4-x}(OH₂⁺)_x framework was formed due to the incomplete hydrolysis and condensation of TTIP/TiCl₄ under acidic condition, and then it interacted with surfactant P123 or F127 to form the semi-transparent sol of H₃PW₁₂O₄₀/Ti(Oi-Pr)_{4-x}(OH₂⁺)_x-EO₂₀PO₇₀EO₂₀ or H₃PW₁₂O₄₀/Ti(Oi-Pr)_{4-x}(OH₂⁺)_x-EO₁₀₆PO₇₀EO₁₀₆ inorganic-organic framework through hydrogen bonding. TiCl₄ added in the current preparation system is as the pH “adjustor”, hydrolysis-condensation “controller” as well as titanium source, while TTIP was used as a titanium source only. Subsequently, half of the above sol was treated by EISA strategy. During EtOH evaporation slowly at 40 °C, inorganic precursors further hydrolyzed and cross-linked to yield H₃PW₁₂O₄₀/(OH)_{4-n}Ti(OTi)_n-EO₂₀PO₇₀EO₂₀ or H₃PW₁₂O₄₀/(OH)_{4-n}Ti(OTi)_n-EO₁₀₆PO₇₀EO₁₀₆ framework; simultaneously, the highly concentrated surfactant self-assembled into lyotropic liquid-crystalline phase and then the ordered mesostructure can be fabricated. The mesophase was solidified by subsequent low-temperature thermal treatment (120 °C). After hot ethanol extraction the templates can be easily removed, creating H₃PW₁₂O₄₀/TiO₂ material with ordered accessible pores of uniform size and arrangement. Further calcination of the product at 350 °C led to the material in an anatase phase structure (see Figs. 1 and 2). Interestingly, for as-prepared ordered mesoporous H₃PW₁₂O₄₀/TiO₂ materials, their pore dimensions can be adjusted by using different triblock copolymer surfactants. That is, 2D hexagonal phase and 3D cubic structure can be obtained by using P123 and F127 as the template, respectively (see Figs. 1 and 2).

The other half of the H₃PW₁₂O₄₀/Ti(Oi-Pr)_{4-x}(OH₂⁺)_x-EO₂₀PO₇₀EO₂₀ or H₃PW₁₂O₄₀/Ti(Oi-Pr)_{4-x}(OH₂⁺)_x-EO₁₀₆PO₇₀EO₁₀₆ sol was subjected to hydrothermal treatment at 150 °C and then dehydration at 60 °C. After the above two steps, H₃PW₁₂O₄₀/(OH)_{4-n}Ti(OTi)_n-EO₂₀PO₇₀EO₂₀ or H₃PW₁₂O₄₀/(OH)_{4-n}Ti(OTi)_n-EO₁₀₆PO₇₀EO₁₀₆ framework was obtained. This mesophase was reinforced by low-temperature thermal treatment (120 °C). Subsequent hot ethanol extraction resulted in H₃PW₁₂O₄₀/TiO₂ powder with 3D interconnected sponge-like mesostructure regardless of P123 and F127 being applied (see Fig. 1); moreover, the powders exhibited anatase phase although no further calcination was applied (see Fig. 1d). The result implies that current hydrothermal treatment destructed the environment of surfactant self-assembling into lyotropic liquid-crystalline phase, leading to the products without structural ordering.

3.2. Characterization

3.2.1. Mesostructure, morphology, and porosity

The morphology, structural ordering, and phase structure of as-prepared H₃PW₁₂O₄₀/TiO₂ materials were characterized by HRTEM, and SAXS and WXR analysis. The representative HRTEM images of H₃PW₁₂O₄₀/TiO₂ materials prepared via the different routes are shown in Fig. 1. Fig. 1a reveals that the P123-templated H₃PW₁₂O₄₀/TiO₂ materials obtained via EISA route possess 2D hexagonal pore morphology with pore diameter lower than 5 nm. Therefore, these materials were denoted as H₃PW₁₂O₄₀/TiO₂-2D_{hex}. Fig. 2b indicates the F127-templated H₃PW₁₂O₄₀/TiO₂ samples obtained via EISA route shows the regular arrangement of the pores along various plane directions, implying that the samples possess a 3D cubic mesostructure with pore diameter lower than 5 nm. Therefore, these materials were denoted as H₃PW₁₂O₄₀/TiO₂-3D_{cub}. As for two hydrothermal treatment-prepared samples, sponge-like disordered 3D interconnected mesostructures were observed regardless of using P123 (denoted as

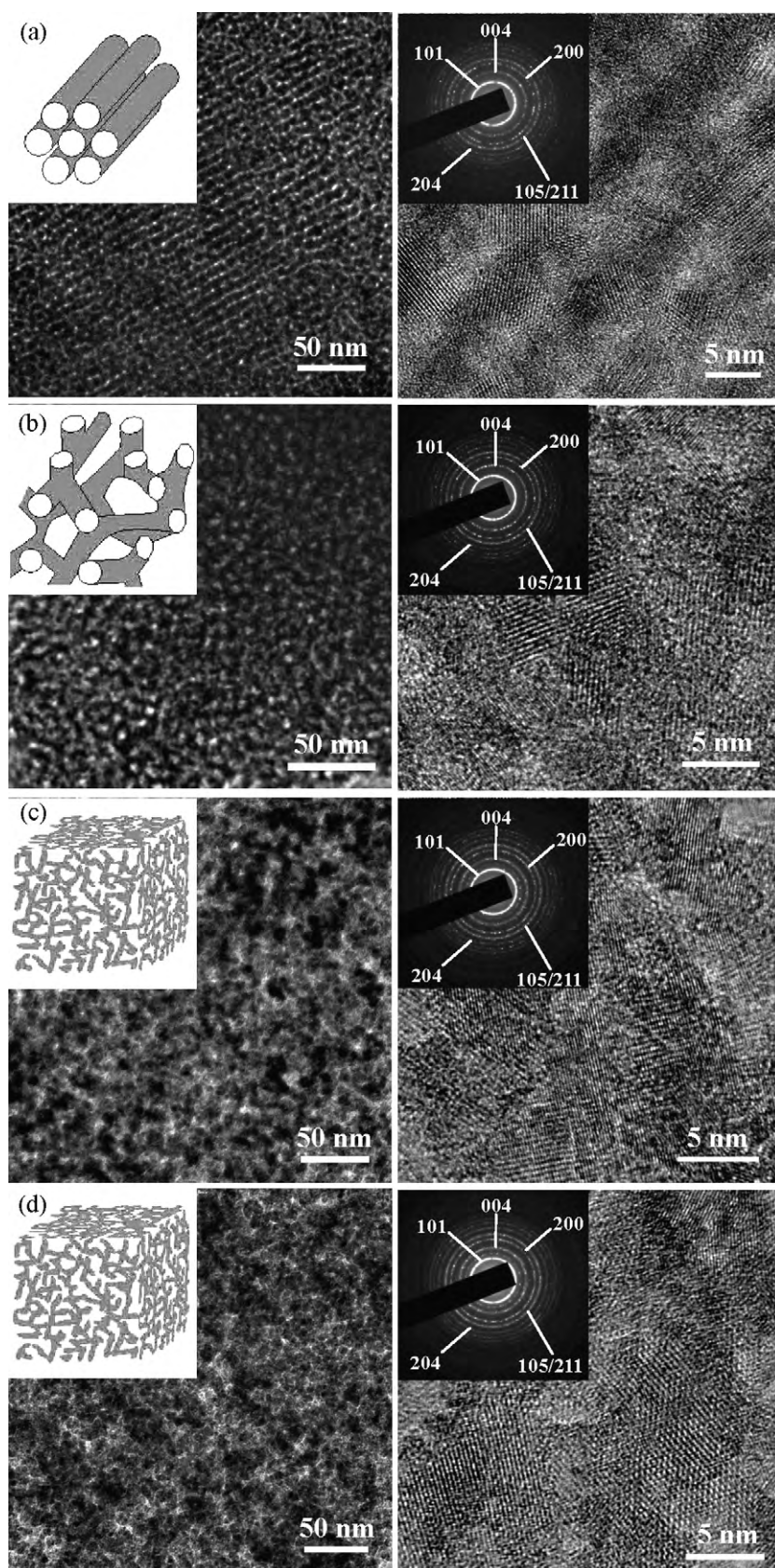


Fig. 1. TEM, HRTEM, and SAED images of $\text{H}_3\text{PW}_{12}\text{O}_{40}/\text{TiO}_2\text{-}2\text{D}_{\text{hex}}\text{-}14.5$ (a), $\text{H}_3\text{PW}_{12}\text{O}_{40}/\text{TiO}_2\text{-}3\text{D}_{\text{cub}}\text{-}13.1$ (b), $\text{H}_3\text{PW}_{12}\text{O}_{40}/\text{TiO}_2\text{-}3\text{D}_{\text{spo-1}}\text{-}12.3$ (c), and $\text{H}_3\text{PW}_{12}\text{O}_{40}/\text{TiO}_2\text{-}3\text{D}_{\text{spo-2}}\text{-}12.7$ (d).

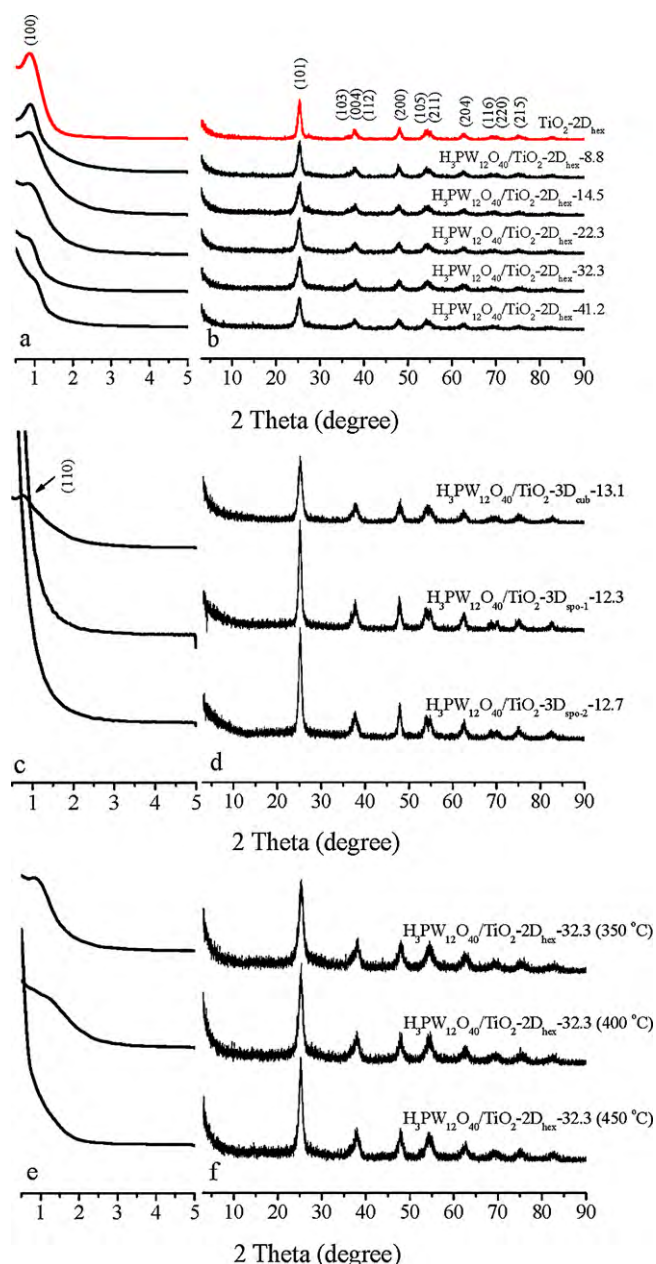


Fig. 2. Small angle X-ray scattering (SAXS) and wide angle X-ray diffraction (WAXD) patterns of mesoporous TiO_2 and $\text{H}_3\text{PW}_{12}\text{O}_{40}/\text{TiO}_2$ materials with 2D hexagonal (a, b, e, and f), 3D cubic (c and d), and 3D sponge-like (c and d) pore morphology.

$\text{H}_3\text{PW}_{12}\text{O}_{40}/\text{TiO}_2\text{-}3\text{D}_{\text{spo-1}}$) or F127 (denoted as $\text{H}_3\text{PW}_{12}\text{O}_{40}/\text{TiO}_2\text{-}3\text{D}_{\text{spo-2}}$) as a template (Fig. 1c and d). Although it is difficult to estimate the pore diameter of these two samples accurately from their TEM images owing to the interconnected structure, pore diameter of $\text{H}_3\text{PW}_{12}\text{O}_{40}/\text{TiO}_2\text{-}3\text{D}_{\text{spo-1}}$ or $\text{H}_3\text{PW}_{12}\text{O}_{40}/\text{TiO}_2\text{-}3\text{D}_{\text{spo-2}}$ sample is larger than that of $\text{H}_3\text{PW}_{12}\text{O}_{40}/\text{TiO}_2\text{-}2\text{D}_{\text{hex}}$ or $\text{H}_3\text{PW}_{12}\text{O}_{40}/\text{TiO}_2\text{-}3\text{D}_{\text{cub}}$ sample; moreover, pore diameter of the $\text{H}_3\text{PW}_{12}\text{O}_{40}/\text{TiO}_2\text{-}3\text{D}_{\text{spo-1}}$ sample is smaller than that of the $\text{H}_3\text{PW}_{12}\text{O}_{40}/\text{TiO}_2\text{-}3\text{D}_{\text{spo-2}}$ sample. The nanocrystalline nature of the material is visibly observed in its corresponding HRTEM image. The lattice fringe that is used for phase determination is 0.35 nm, corresponding to the lattice spacing of (1 0 1) plane in the anatase phase. The selected area electron diffraction (SAED) patterns of the materials further confirm the anatase structure of the $\text{H}_3\text{PW}_{12}\text{O}_{40}/\text{TiO}_2$ materials, and the rings from the inner to the outer correspond to

(1 0 1), (0 0 4), (2 0 0), (1 0 5/2 1 1), and (2 0 4) diffraction of anatase phase (inserts in Fig. 1) [39].

The SAXS results are consistent with those of the above TEM observation. The SAXS patterns of the $\text{H}_3\text{PW}_{12}\text{O}_{40}/\text{TiO}_2\text{-}2\text{D}_{\text{hex}}$ samples shown in Fig. 1a exhibit the peak at ca. 0.9° (1 0 0), indicating that the materials tailored by P123 exhibit ordered mesostructure. However, as increase $\text{H}_3\text{PW}_{12}\text{O}_{40}$ loading from 0% to 41.2%, the peak intensity decrease gradually, suggesting that the ordered mesostructure was partially destructed by incorporating the Keggin unit with higher loading. Similar results are obtained for the F127-tailored and EISA-prepared $\text{H}_3\text{PW}_{12}\text{O}_{40}/\text{TiO}_2$ sample (Fig. 1c), and its scattering peak appears at ca. 0.8° (1 1 0). Nevertheless, the pore ordering of the $\text{H}_3\text{PW}_{12}\text{O}_{40}/\text{TiO}_2\text{-}2\text{D}_{\text{hex}}$ or $\text{H}_3\text{PW}_{12}\text{O}_{40}/\text{TiO}_2\text{-}3\text{D}_{\text{cub}}$ is relatively low due to the lack of other two weak peaks in the range of $1.2\text{--}1.8^\circ$ for $\text{H}_3\text{PW}_{12}\text{O}_{40}/\text{TiO}_2\text{-}2\text{D}_{\text{hex}}$ and $1.0\text{--}1.5^\circ$ for $\text{H}_3\text{PW}_{12}\text{O}_{40}/\text{TiO}_2\text{-}3\text{D}_{\text{cub}}$, and therefore it is difficult to distinguish the pore dimension of the above two types of the samples only based on SAXS results [40].

As for the other two $\text{H}_3\text{PW}_{12}\text{O}_{40}/\text{TiO}_2$ samples prepared by a hydrothermal treatment route, $\text{H}_3\text{PW}_{12}\text{O}_{40}/\text{TiO}_2\text{-}3\text{D}_{\text{spo-1}}$ and $\text{H}_3\text{PW}_{12}\text{O}_{40}/\text{TiO}_2\text{-}3\text{D}_{\text{spo-2}}$, the scattering peaks in small angle range were failed to be detected, indicating the disordered mesophase structure of the samples (Fig. 1c). In the cases of the 400°C calcined $\text{H}_3\text{PW}_{12}\text{O}_{40}/\text{TiO}_2\text{-}2\text{D}_{\text{hex}}\text{-}32.3$ sample, its SAXS peak became ambiguous. Further increase the calcination temperature to 450°C , this peak disappeared (Fig. 1e). The result suggests that calcination of the $\text{H}_3\text{PW}_{12}\text{O}_{40}/\text{TiO}_2$ material at higher temperature result in disordered mesophase owing to pore collapse.

The WAXRD patterns confirm that all the tested $\text{H}_3\text{PW}_{12}\text{O}_{40}/\text{TiO}_2$ samples, regardless of the preparation routes, possess pure anatase phase with characteristic diffractions at 25.2° (1 0 1), 37.8° (1 0 3, 0 0 4, and 1 1 2), 48.1° (2 0 0), 54.7° (1 0 5, 2 1 1), 62.7° (2 0 4), 69.9° (1 1 6, 2 2 0), and 75.3° (2 1 5), respectively (Fig. 1b, d, and f; JCPDS No. 21-1272). Additionally, the diffractions related to the Keggin unit were not found, implying homogeneous dispersion of the Keggin unit throughout the materials even $\text{H}_3\text{PW}_{12}\text{O}_{40}$ loading is as high as 41.2%. From WAXRD patterns it also can be found that the crystallinity of the samples prepared by hydrothermal treatment ($\text{H}_3\text{PW}_{12}\text{O}_{40}/\text{TiO}_2\text{-}3\text{D}_{\text{spo-1}}$ or $\text{H}_3\text{PW}_{12}\text{O}_{40}/\text{TiO}_2\text{-}3\text{D}_{\text{spo-2}}$) is higher with respect to the EISA-prepared sample.

The nitrogen adsorption/desorption isotherms of as-prepared TiO_2 and $\text{H}_3\text{PW}_{12}\text{O}_{40}/\text{TiO}_2$ materials are type IV with an H2 hysteresis loop, characteristic of mesoporous materials tailored by nonionic-surfactants (Fig. 3a and c). The capillary condensation occurs at a relative pressure of 0.45–0.75 for the 2D ordered $\text{H}_3\text{PW}_{12}\text{O}_{40}/\text{TiO}_2$ materials (Fig. 3a), and BJH desorption pore distribution analysis shows that the pore diameters of these materials are quite uniform (Fig. 3b). As for the ordered and disordered 3D $\text{H}_3\text{PW}_{12}\text{O}_{40}/\text{TiO}_2$ materials, the capillary condensation occurs at different relative pressure regions (Fig. 3c). For EISA-prepared 3D $\text{H}_3\text{PW}_{12}\text{O}_{40}/\text{TiO}_2$ material ($\text{H}_3\text{PW}_{12}\text{O}_{40}/\text{TiO}_2\text{-}3\text{D}_{\text{cub}}$), its capillary condensation occurs at a relative pressure of 0.45–0.75 region with narrow pore size distribution (Fig. 3d). However, the onset of the capillary condensation step occurs at higher relative pressure (starting from 0.70) for the hydrothermal treatment-prepared 3D $\text{H}_3\text{PW}_{12}\text{O}_{40}/\text{TiO}_2$ materials ($\text{H}_3\text{PW}_{12}\text{O}_{40}/\text{TiO}_2\text{-}3\text{D}_{\text{spo-1}}$ and $\text{H}_3\text{PW}_{12}\text{O}_{40}/\text{TiO}_2\text{-}3\text{D}_{\text{spo-2}}$), implying enlarged pore size with respect to EISA-prepared 3D $\text{H}_3\text{PW}_{12}\text{O}_{40}/\text{TiO}_2$ materials. The result is consistent with BJH desorption pore distribution curve and pore diameters calculated by the BJH method on the desorption branch of the N_2 sorption isotherms (Table 1). Larger pore diameter of $\text{H}_3\text{PW}_{12}\text{O}_{40}/\text{TiO}_2\text{-}3\text{D}_{\text{spo-2}}\text{-}12.7$ (13.2 nm) compared with $\text{H}_3\text{PW}_{12}\text{O}_{40}/\text{TiO}_2\text{-}3\text{D}_{\text{spo-1}}\text{-}12.3$ (10.7 nm) is due to the molecule size of F127 is larger than that of P123. Additionally, pore size distribution for the hydrothermal treatment-prepared 3D $\text{H}_3\text{PW}_{12}\text{O}_{40}/\text{TiO}_2$ materials is much wider compared with the EISA-prepared mate-

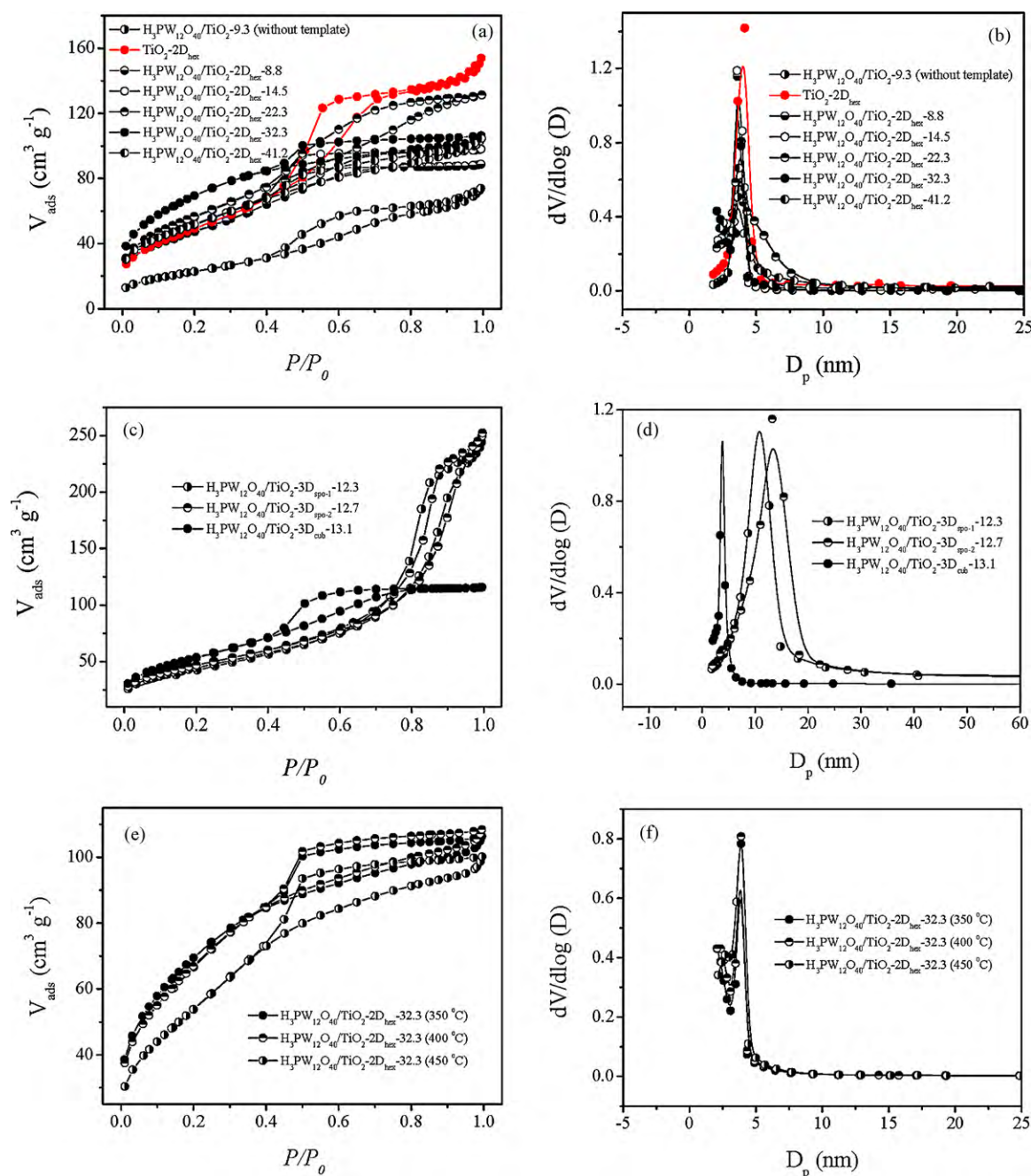


Fig. 3. Nitrogen adsorption/desorption isotherms and pore size distribution profiles of mesoporous TiO_2 and $\text{H}_3\text{PW}_{12}\text{O}_{40}/\text{TiO}_2$ materials with 2D hexagonal (a, b, e, and f), 3D cubic (c and d), and 3D sponge-like (c and d) pore morphology. (For interpretation of the references to colour in this figure, the reader is referred to the web version of the article.)

material, indicating that the pore diameters of these materials are less uniform. Among all tested mesoporous $\text{H}_3\text{PW}_{12}\text{O}_{40}/\text{TiO}_2$ materials, two hydrothermal treatment-prepared 3D disordered $\text{H}_3\text{PW}_{12}\text{O}_{40}/\text{TiO}_2$ materials possess the highest porosity. From the calculated textural parameters summarized in Table 1 it is found that the BET surface areas of the $\text{H}_3\text{PW}_{12}\text{O}_{40}/\text{TiO}_2$ materials is mainly affected by $\text{H}_3\text{PW}_{12}\text{O}_{40}$ loading: for the tested $\text{H}_3\text{PW}_{12}\text{O}_{40}/\text{TiO}_2\text{-2D}_{\text{hex}}$ materials, the BET surface area increased from $174 \text{ m}^2 \text{ g}^{-1}$ to $255 \text{ m}^2 \text{ g}^{-1}$ as increase $\text{H}_3\text{PW}_{12}\text{O}_{40}$ loading from 8.8% to 32.3%; further increase $\text{H}_3\text{PW}_{12}\text{O}_{40}$ loading to 41.2% resulted in decreased BET surface area ($188 \text{ m}^2 \text{ g}^{-1}$). Additionally, at similar $\text{H}_3\text{PW}_{12}\text{O}_{40}$ loading (12.3–14.5%), ordered mesoporous $\text{H}_3\text{PW}_{12}\text{O}_{40}/\text{TiO}_2$ materials possess similar BET surface area regardless of pore dimensions. In the cases of ordered and disordered 3D

mesoporous $\text{H}_3\text{PW}_{12}\text{O}_{40}/\text{TiO}_2$ materials with similar $\text{H}_3\text{PW}_{12}\text{O}_{40}$ loading, the BET surface area of the former is higher somewhat. Finally, the influence of the calcination temperature on the textural properties of as-prepared materials was tested by the representative sample, $\text{H}_3\text{PW}_{12}\text{O}_{40}/\text{TiO}_2\text{-2D}_{\text{hex}}\text{-32.3}$ (Fig. 3e and f). It shows that the mesoporosity of the materials still remained as increase the calcination temperature from 350°C to 450°C ; however, the adsorption capacity to nitrogen and porosity decreased accompanying with the decreased BET surface area (Table 1).

3.2.2. Optical absorption properties

It is well-known that, in addition to the crystal phase structure, the band electronic structure of a photocatalytic material (which determines its band gap energy) usually plays a dominant role in its

Table 1
Textural parameters of mesoporous TiO₂ and H₃PW₁₂O₄₀/TiO₂ materials.

Sample	D_p (nm) ^a	V_p (cm ³ g ⁻¹) ^b	S_{BET} (m ² g ⁻¹)
TiO ₂ -2D _{hex}	4.1	0.22	182
H ₃ PW ₁₂ O ₄₀ /TiO ₂ -2D _{hex} -8.8	3.6	0.14	174
H ₃ PW ₁₂ O ₄₀ /TiO ₂ -2D _{hex} -14.5	3.6	0.15	190
H ₃ PW ₁₂ O ₄₀ /TiO ₂ -2D _{hex} -22.3	3.9	0.20	208
H ₃ PW ₁₂ O ₄₀ /TiO ₂ -2D _{hex} -32.3 (350 °C)	3.9	0.16	255
H ₃ PW ₁₂ O ₄₀ /TiO ₂ -2D _{hex} -32.3 (400 °C)	3.9	0.16	247
H ₃ PW ₁₂ O ₄₀ /TiO ₂ -2D _{hex} -32.3 (450 °C)	4.0	0.15	199
H ₃ PW ₁₂ O ₄₀ /TiO ₂ -2D _{hex} -41.2	3.7	0.15	188
H ₃ PW ₁₂ O ₄₀ /TiO ₂ -3D _{cub} -13.1	3.8	0.18	197
H ₃ PW ₁₂ O ₄₀ /TiO ₂ -3D _{spo-1} -12.3	10.7	0.36	162
H ₃ PW ₁₂ O ₄₀ /TiO ₂ -3D _{spo-2} -12.7	13.2	0.37	170
H ₃ PW ₁₂ O ₄₀ /TiO ₂ -9.3 (without template)	3.6	0.11	85

^a D_p (pore diameter) was estimated from BJH desorption determination.

^b V_p (pore volume) was estimated from the pore volume determined using the adsorption branch of the nitrogen isotherm curve at $P/P_0 = 0.98$ single point.

photocatalytic activity. Herein, the influence of the introduction of the Keggin unit into TiO₂ matrix on the band gap energy of TiO₂ was studied by the optical response of as-prepared H₃PW₁₂O₄₀/TiO₂ materials through UV–Vis/DRS determination. Fig. 4a displays the UV–Vis/DRS of as-prepared H₃PW₁₂O₄₀/TiO₂ materials with various H₃PW₁₂O₄₀ loading (0–41.2%) by using H₃PW₁₂O₄₀/TiO₂-2D_{hex} as the representative samples. It showed that each TiO₂-based material has a band-to-band absorption band edge starting from 260 nm and ending up to ca. 400 nm. Moreover, the band of the H₃PW₁₂O₄₀/TiO₂ materials had a slight redshift compared with

pure TiO₂, but it had somewhat blueshift as increase H₃PW₁₂O₄₀ loading from 8.8% to 41.2%. Fig. 4b compares the difference of the light absorption properties of the H₃PW₁₂O₄₀/TiO₂ materials with different pore geometries and structural orderings, and the results indicate that the influence of the pore geometries and structural orderings on the light absorption properties of the H₃PW₁₂O₄₀/TiO₂ materials is neglectable at similar H₃PW₁₂O₄₀ loading. From Fig. 4 it is also found that no separated absorption peaks corresponding to either H₃PW₁₂O₄₀ or TiO₂ were detected in the H₃PW₁₂O₄₀/TiO₂ materials, and that no absorption tail was found. The result further confirms the Keggin unit homogeneously distributed at the atomic level throughout the whole titania matrix.

For neat TiO₂, the absorption band is originated from the charge transfer from O2p to Ti3d orbit. In the case of the H₃PW₁₂O₄₀/TiO₂ materials, from their optical absorption characteristics shown in Fig. 4 it is inferred that the absorption band of H₃PW₁₂O₄₀/TiO₂ corresponds to the charge transfer from O2p to the new conduction band constructed from the hybridization of Ti3d and W5d orbits of the Keggin unit. The conclusion is reasonable because Ti3d orbits and W5d orbits exhibit similar energy levels [34].

3.2.3. Compositional and structural information

The determined H₃PW₁₂O₄₀ loadings are as expected (Table 1), implying that the preparation methods employed can effectively inhibit the loss of the Keggin unit during the template extraction process. After formation of the H₃PW₁₂O₄₀/TiO₂ materials, structural integrity of the Keggin unit was confirmed by spectroscopic methods including FT-IR, ³¹P MAS NMR, and Raman.

Fig. 5 shows FT-IR spectra of the parent H₃PW₁₂O₄₀ and the representative H₃PW₁₂O₄₀/TiO₂-2D_{hex} materials. For the parent H₃PW₁₂O₄₀, its characteristic frequencies related to the Keggin unit appear at 1079 cm⁻¹, 985 cm⁻¹, 890 cm⁻¹, and 795 cm⁻¹, respectively, attributed to the vibrations of the P–O bonds of the PO₄ units, W=O bonds, and two W–O–W bonds of the Keggin unit. After the formation of the H₃PW₁₂O₄₀/TiO₂ composite materials, the vibrational frequencies change to 1076 cm⁻¹, 981 cm⁻¹, 896 cm⁻¹, and 816 cm⁻¹. The above result implies that the primary Keggin structure remained intact after being introduced into the TiO₂ framework by current preparation route; additionally, the shifts of the frequencies mainly occurred at W–O–W bonds compared with the parent H₃PW₁₂O₄₀, implying strong interaction between the Keggin unit and TiO₂ support at the interface of the two components [42].

³¹P MAS NMR spectrum strongly supports the above results (Fig. 6). The narrow peak at –17.5 ppm (referenced to the resonances of monoammonium phosphate standard) was obtained as expected, originating from the resonance at PO₄ units within the bulk H₃PW₁₂O₄₀ environment.

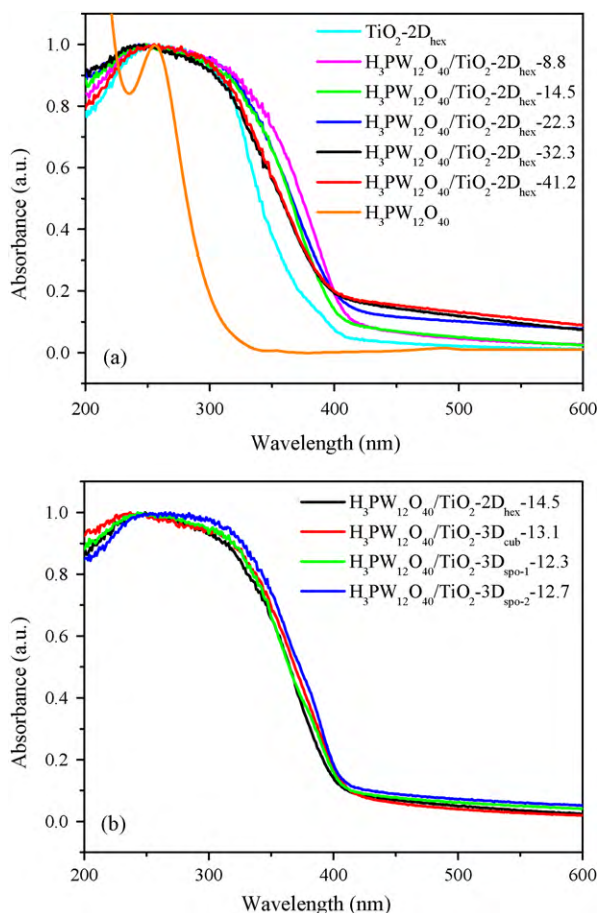


Fig. 4. UV–Vis/DRS of the starting H₃PW₁₂O₄₀, TiO₂, and H₃PW₁₂O₄₀/TiO₂ materials. (a) Different H₃PW₁₂O₄₀ loadings and (b) different pore morphologies. (For interpretation of the references to colour in this figure, the reader is referred to the web version of the article.)

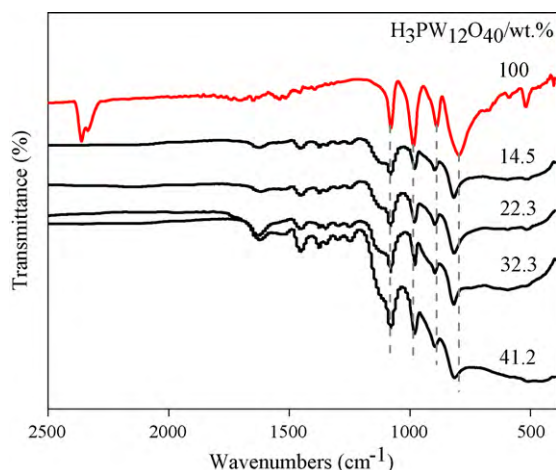


Fig. 5. FT-IR spectra of $\text{H}_3\text{PW}_{12}\text{O}_{40}/\text{TiO}_2\text{-}2\text{D}_{\text{hex}}$ series as a function of $\text{H}_3\text{PW}_{12}\text{O}_{40}$ loading.

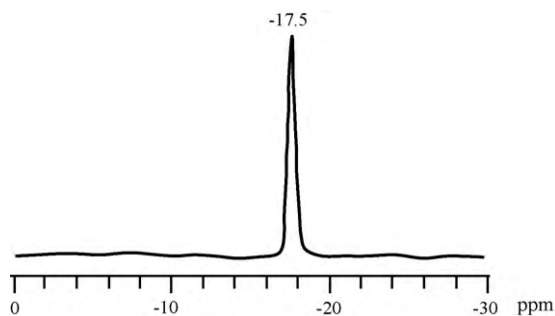


Fig. 6. Room temperature ^{31}P MAS NMR spectrum (referenced to the resonances of monoammonium phosphate standard) of the $\text{H}_3\text{PW}_{12}\text{O}_{40}/\text{TiO}_2\text{-}2\text{D}_{\text{hex}}$ -41.2 material.

Raman scattering spectra of the starting $\text{H}_3\text{PW}_{12}\text{O}_{40}$, TiO_2 , and $\text{H}_3\text{PW}_{12}\text{O}_{40}/\text{TiO}_2$ materials (represented by $\text{H}_3\text{PW}_{12}\text{O}_{40}/\text{TiO}_2\text{-}2\text{D}_{\text{hex}}$) are illustrated in Fig. 7. It shows that the starting $\text{H}_3\text{PW}_{12}\text{O}_{40}$ exhibits three Raman scattering peaks situated at 1008 cm^{-1} , 992 cm^{-1} , and 906 cm^{-1} , corresponding to stretching vibrations of P–O bonds of the PO_4 units, W=O bonds, and W–O–W bonds of the Keggin unit, respectively (Fig. 7a). In the case of as-prepared TiO_2 , four characteristic Raman scattering peaks found at 154 cm^{-1} (E_g), 400 cm^{-1} (B_{1g}), 520 cm^{-1} (B_{1g}), and 646 cm^{-1} (E_g) originated from anatase TiO_2 [41]. After formation of the $\text{H}_3\text{PW}_{12}\text{O}_{40}/\text{TiO}_2$ composite materials, the four anatase TiO_2 -related peaks still can be detected. However, E_g Raman mode at 154 cm^{-1} shifted to lower wavenumbers: for the $\text{H}_3\text{PW}_{12}\text{O}_{40}/\text{TiO}_2\text{-}2\text{D}_{\text{hex}}$ material with $\text{H}_3\text{PW}_{12}\text{O}_{40}$ loading from 8.8%, 14.5%, 22.3%, 32.3%, to 41.2%, this Raman mode shifts to 151 cm^{-1} , 151 cm^{-1} , 151 cm^{-1} , 148 cm^{-1} , and 148 cm^{-1} , respectively (Fig. 7b). As for the Keggin unit-related peaks in the composite materials, the above three peaks corresponding to the vibrations of W–O–W, W=O, and P–O bonds were broadened and weakened, therefore, we only observed one wide peak in the range of $977\text{--}1026\text{ cm}^{-1}$ with $\text{H}_3\text{PW}_{12}\text{O}_{40}$ loading from 8.8% to 41.2%. The above result implies that strong interactions existed between the Keggin unit and TiO_2 support also changed symmetry somewhat of W–O–W bonds or W=O bonds.

Raman spectroscopy can also be a powerful tool for detecting the surface defects of anatase matrix due to the incorporation of the Keggin unit, which strongly affect the surface of the photocatalysts [15]. The surface defects of anatase matrix are frequently featured by the shifts of Raman active modes. For the $\text{H}_3\text{PW}_{12}\text{O}_{40}/\text{TiO}_2\text{-}2\text{D}_{\text{hex}}$ materials, the shift of E_g mode at 154 cm^{-1} towards lower

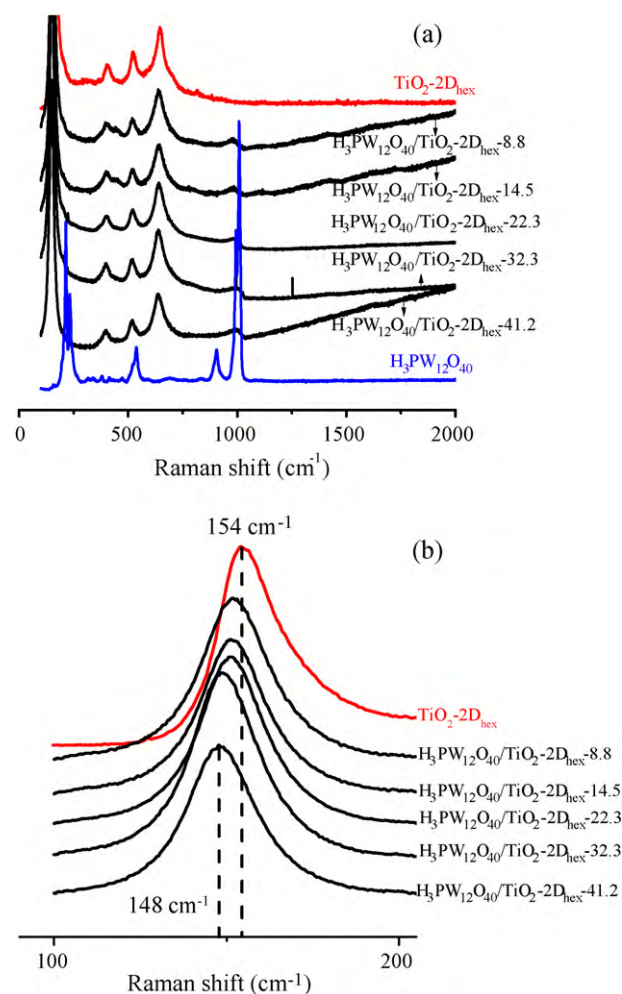
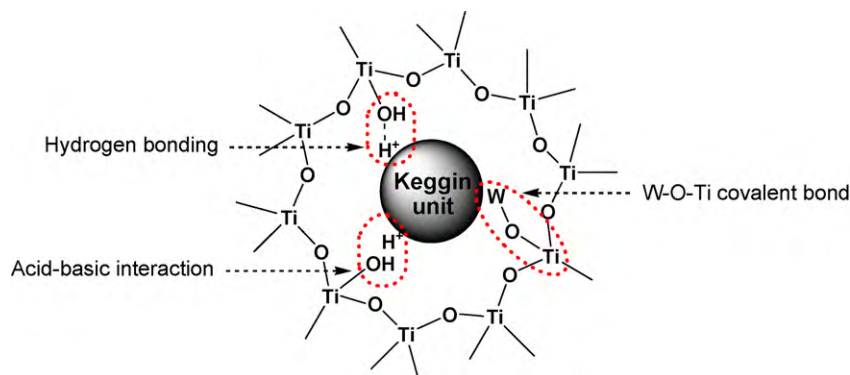


Fig. 7. Raman scattering spectra of the starting $\text{H}_3\text{PW}_{12}\text{O}_{40}$, TiO_2 , and $\text{H}_3\text{PW}_{12}\text{O}_{40}/\text{TiO}_2$ materials. (a) $100\text{--}2000\text{ cm}^{-1}$ and (b) $100\text{--}250\text{ cm}^{-1}$.

wavenumber is caused by the altered symmetry of the doped Ti–O–Ti network, implying slight change of surface structures of anatase owing to the introduction of the Keggin unit. The above spectroscopy characterization is consistent with our previous XPS surface probe results. That is, some shifts of $\text{Ti}2\text{p}$ and $\text{W}4\text{f}$ binding energies in the $\text{H}_3\text{PW}_{12}\text{O}_{40}/\text{TiO}_2$ materials compared with pure TiO_2 indicate that a slight perturbation of Ti or W environment at the interface between the Keggin unit and anatase matrix [42].

Based on the spectroscopy characterization and XPS analysis together with well-matched electronegativity and ionic radius of Ti^{4+} ion ($1.54, 0.0605\text{ nm}$) and W^{6+} ion ($1.70, 0.060\text{ nm}$), it is inferred that in the $\text{H}_3\text{PW}_{12}\text{O}_{40}/\text{TiO}_2$ materials the Keggin units link with the TiO_2 support through W–O–Ti covalent bonds formed due to the interactions between the terminal W=O bonds or bridge W–O–Ti bonds within the Keggin units and the surface $\equiv\text{Ti}\text{--OH}$ groups within anatase TiO_2 matrix. Similar results have also been reported by our previous work [43] and other groups' studies [44]. Additionally, hydrogen bonding and acid–base interactions between the oxygen atoms of the Keggin anion and the surface $\equiv\text{Ti}\text{--OH}$ groups of anatase TiO_2 may also exist in the composites. These strong bonding between the two components inhibited the drop of the Keggin unit from TiO_2 matrix during the $\text{H}_3\text{PW}_{12}\text{O}_{40}/\text{TiO}_2$ preparation procedure and subsequent catalytic tests. The proposed network structure of the $\text{H}_3\text{PW}_{12}\text{O}_{40}/\text{TiO}_2$ material (it constructs the wall component of the material) is displayed in Scheme 1 according to the above discussion.



Scheme 1. The wall component of the mesoporous $\text{H}_3\text{PW}_{12}\text{O}_{40}/\text{TiO}_2$ materials.

3.3. Photocatalytic tests

3.3.1. Adsorption and photocatalytic degradation of DEP

Adsorption capacity and photocatalytic activity of as-prepared $\text{H}_3\text{PW}_{12}\text{O}_{40}/\text{TiO}_2$ materials were studied by selecting DEP as a target compound; meanwhile, the influences of $\text{H}_3\text{PW}_{12}\text{O}_{40}$ loadings, mesostructural orderings and pore geometries, and calcination temperature on the photocatalytic activity of $\text{H}_3\text{PW}_{12}\text{O}_{40}/\text{TiO}_2$ were discussed. The photocatalytic tests were run in an aqueous solution containing molecule oxygen from air dissolved in solution. And light irradiation was provided by solar simulating Xe lamp at $\lambda > 320 \text{ nm}$ (near UV-light area) and $\lambda > 400 \text{ nm}$ (visible-light area), respectively. Direct photolysis experiment indicates that change of the concentration of DEP in the reaction system is neglectable under near UV-light irradiation for 60 min (Fig. 8a).

Adsorption tests showed that: (i) it took 30 min before adsorption–desorption equilibrium is reached; (ii) for the $\text{H}_3\text{PW}_{12}\text{O}_{40}/\text{TiO}_2\text{-}2\text{D}_{\text{hex}}$ materials, they showed similar adsorption capacity to DEP molecules regardless of $\text{H}_3\text{PW}_{12}\text{O}_{40}$ loading (Fig. 8a); (iii) 3D interconnected $\text{H}_3\text{PW}_{12}\text{O}_{40}/\text{TiO}_2$ material showed slightly higher adsorption capacity compared with ordered 2D or 3D $\text{H}_3\text{PW}_{12}\text{O}_{40}/\text{TiO}_2$ material at similar $\text{H}_3\text{PW}_{12}\text{O}_{40}$ loading (Fig. 8b). This is owing to the higher porosity of 3D interconnected $\text{H}_3\text{PW}_{12}\text{O}_{40}/\text{TiO}_2$ material; and (iv) $\text{H}_3\text{PW}_{12}\text{O}_{40}/\text{TiO}_2\text{-}2\text{D}_{\text{hex}}$ material obtained at lower calcined temperature showed somewhat higher adsorption capacity compared with the materials obtained at higher calcination temperature (Fig. 8c), attributed to larger BET surface area of the former with respect to the latter.

The photocatalytic activity of the $\text{H}_3\text{PW}_{12}\text{O}_{40}/\text{TiO}_2$ materials was firstly tested by the $\text{H}_3\text{PW}_{12}\text{O}_{40}/\text{TiO}_2\text{-}2\text{D}_{\text{hex}}$ materials

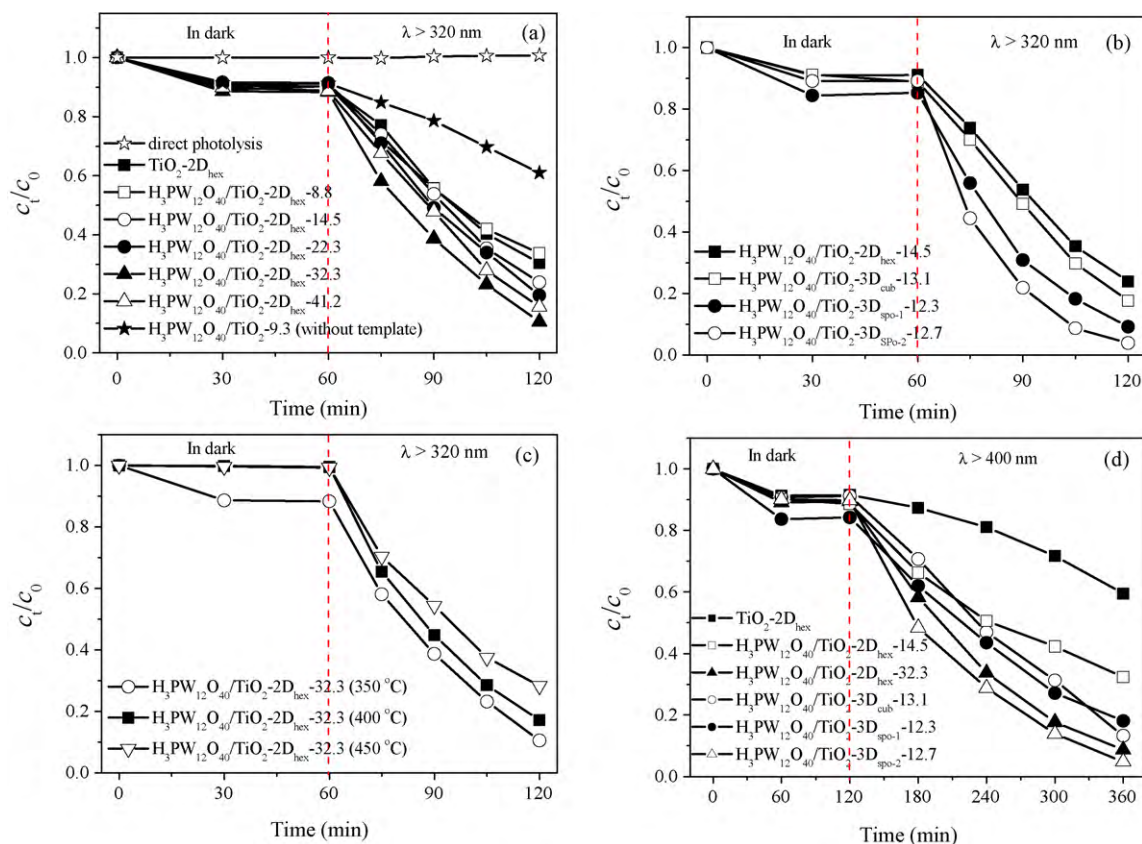


Fig. 8. Photocatalytic activity of mesoporous TiO_2 and $\text{H}_3\text{PW}_{12}\text{O}_{40}/\text{TiO}_2$ materials towards DEP degradation. (a) Influence of $\text{H}_3\text{PW}_{12}\text{O}_{40}$ loadings, (b) influence of pore morphologies, (c) Influence of the catalyst calcination temperatures, and (d) irradiation at $\lambda > 400 \text{ nm}$. Initial concentration of DEP 13.5 mg L^{-1} , volume 100 mL, catalyst amount 150 mg.

with $\text{H}_3\text{PW}_{12}\text{O}_{40}$ loadings from 0% to 41.2%. For comparison, $\text{H}_3\text{PW}_{12}\text{O}_{40}/\text{TiO}_2$ -9.3 (without template) sample was also tested under the same conditions. From the results displayed in Fig. 8a it is found that the photocatalytic activity of the $\text{H}_3\text{PW}_{12}\text{O}_{40}/\text{TiO}_2$ -2D_{hex} materials to DEP degradation monotonically increased with the increase of $\text{H}_3\text{PW}_{12}\text{O}_{40}$ doping from 8.8% to 32.3%. Further increase $\text{H}_3\text{PW}_{12}\text{O}_{40}$ loading to 41.2% caused a slight decreased photocatalytic activity. For example, $\text{H}_3\text{PW}_{12}\text{O}_{40}/\text{TiO}_2$ -2D_{hex}-32.3 is the most photoactive among all tested materials, and degradation of DEP reached to 89.5% after exposure UV-light irradiation ($\lambda > 320$ nm) for 60 min. Additionally, for the $\text{H}_3\text{PW}_{12}\text{O}_{40}/\text{TiO}_2$ materials with $\text{H}_3\text{PW}_{12}\text{O}_{40}$ loading higher than 8.8%, their photocatalytic activity is higher than pure TiO_2 . As for the $\text{H}_3\text{PW}_{12}\text{O}_{40}/\text{TiO}_2$ -9.3 (without template) sample, its photocatalytic activity to DEP degradation is the lowest among all tested materials. The result implies that adding P123/F127 template or not during $\text{H}_3\text{PW}_{12}\text{O}_{40}/\text{TiO}_2$ material preparation process can affect its photocatalytic activity through tailoring its textural and morphological properties.

Fig. 8b displays the influences of the mesostructural orderings and pore geometries on the photocatalytic activity of $\text{H}_3\text{PW}_{12}\text{O}_{40}/\text{TiO}_2$ materials with similar $\text{H}_3\text{PW}_{12}\text{O}_{40}$ loading (12.3–14.5%). For the ordered 3D and 2D mesoporous $\text{H}_3\text{PW}_{12}\text{O}_{40}/\text{TiO}_2$ material, $\text{H}_3\text{PW}_{12}\text{O}_{40}/\text{TiO}_2$ -3D_{cub}-13.1 and $\text{H}_3\text{PW}_{12}\text{O}_{40}/\text{TiO}_2$ -2D_{hex}-14.5, the former showed higher activity to DEP degradation, i.e., after 60 min UV-light irradiation ($\lambda > 320$ nm) degradation of DEP reached to 82.3% and 76.1%, respectively. As for three 3D mesoporous $\text{H}_3\text{PW}_{12}\text{O}_{40}/\text{TiO}_2$ materials, their activity followed the order $\text{H}_3\text{PW}_{12}\text{O}_{40}/\text{TiO}_2$ -3D_{spo-2}-12.7 > $\text{H}_3\text{PW}_{12}\text{O}_{40}/\text{TiO}_2$ -3D_{spo-1}-12.3 > $\text{H}_3\text{PW}_{12}\text{O}_{40}/\text{TiO}_2$ -3D_{cub}-13.1. After 60 min UV-light irradiation degradation of DEP reached to 96.1% ($\text{H}_3\text{PW}_{12}\text{O}_{40}/\text{TiO}_2$ -3D_{spo-2}-12.7), 90.8% ($\text{H}_3\text{PW}_{12}\text{O}_{40}/\text{TiO}_2$ -3D_{spo-1}-12.3), and 82.3% ($\text{H}_3\text{PW}_{12}\text{O}_{40}/\text{TiO}_2$ -3D_{cub}-13.1), respectively. Therefore, it is concluded 3D disordered $\text{H}_3\text{PW}_{12}\text{O}_{40}/\text{TiO}_2$ materials showed the highest photocatalytic activity among all tested photocatalysts with ordered and disordered 2D or 3D pore morphologies.

Fig. 8c displays the influence of the catalyst calcination temperatures on the photocatalytic activity of $\text{H}_3\text{PW}_{12}\text{O}_{40}/\text{TiO}_2$ materials by using $\text{H}_3\text{PW}_{12}\text{O}_{40}/\text{TiO}_2$ -2D_{hex}-32.3 as a representative catalyst. It is observed that the photocatalytic activity was reduced as increasing the calcination temperature from 350 °C to 450 °C.

Finally, the visible-light ($\lambda > 400$ nm) photocatalytic activity of as-prepared $\text{H}_3\text{PW}_{12}\text{O}_{40}/\text{TiO}_2$ materials to DEP degradation was evaluated, and the results are illustrated in Fig. 8d. It showed that all tested $\text{H}_3\text{PW}_{12}\text{O}_{40}/\text{TiO}_2$ materials exhibit significantly higher visible-light photocatalytic activity with respect to pure TiO_2 . And for the $\text{H}_3\text{PW}_{12}\text{O}_{40}/\text{TiO}_2$ -2D_{hex} materials, higher $\text{H}_3\text{PW}_{12}\text{O}_{40}$ loading exhibits higher visible-light photocatalytic activity. Additionally, at similar $\text{H}_3\text{PW}_{12}\text{O}_{40}$ loading, 3D $\text{H}_3\text{PW}_{12}\text{O}_{40}/\text{TiO}_2$ materials, regardless of structural ordering, show higher visible-light photocatalytic activity than that of 2D ordered $\text{H}_3\text{PW}_{12}\text{O}_{40}/\text{TiO}_2$ material. Certainly, compared to DEP degradation rate under UV-light irradiation, all catalysts show obviously slow degradation rate under visible-light irradiation. For the most active catalyst, $\text{H}_3\text{PW}_{12}\text{O}_{40}/\text{TiO}_2$ -3D_{spo-2}-12.7, it can decompose 95.2% of DEP after exposure to visible-light irradiation for 240 min.

3.3.2. Mineralization of DEP

The mineralization ability of the $\text{H}_3\text{PW}_{12}\text{O}_{40}/\text{TiO}_2$ materials to DEP molecules was evaluated by monitoring the changes of TOC in the reaction systems, and $\text{H}_3\text{PW}_{12}\text{O}_{40}/\text{TiO}_2$ -3D_{spo-2}-12.7 and $\text{H}_3\text{PW}_{12}\text{O}_{40}/\text{TiO}_2$ -2D_{hex}-32.3 materials were chosen as the representative catalysts. For comparison, TiO_2 -2D_{hex} was also tested under the same conditions. From the result illustrated in Fig. 9 it can be seen that the mineralization of DEP over

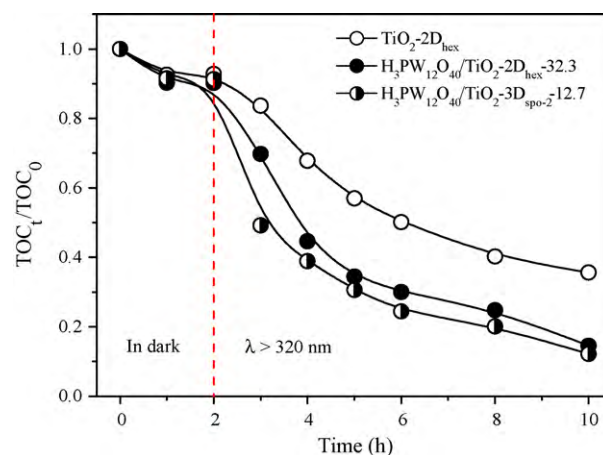


Fig. 9. Evolution of TOC during the course of photocatalytic degradation of aqueous DEP over mesoporous TiO_2 and $\text{H}_3\text{PW}_{12}\text{O}_{40}/\text{TiO}_2$ materials. Simulated sunlight irradiation with $\lambda > 320$ nm, initial concentration of DEP 13.5 mg L⁻¹, volume 100 mL, catalyst amount 150 mg.

the $\text{H}_3\text{PW}_{12}\text{O}_{40}/\text{TiO}_2$ is fast compared with pure TiO_2 . However, mineralization of DEP is slower than its degradation. For example, TOC still remained 49.2% ($\text{H}_3\text{PW}_{12}\text{O}_{40}/\text{TiO}_2$ -3D_{spo-2}-12.7) and 69.8% ($\text{H}_3\text{PW}_{12}\text{O}_{40}/\text{TiO}_2$ -2D_{hex}-32.3) of that of its initial value after DEP disappeared completely. The results imply that some organic intermediates were produced during the DEP degradation course. After exposure to UV-light irradiation for 480 min, 87.8% ($\text{H}_3\text{PW}_{12}\text{O}_{40}/\text{TiO}_2$ -3D_{spo-2}-12.7) and 85.5% ($\text{H}_3\text{PW}_{12}\text{O}_{40}/\text{TiO}_2$ -2D_{hex}-32.3) of TOC disappeared, respectively, indicating that most of the organic intermediates were decomposed and the mineralization of DEP approached completion.

3.3.3. Recyclability of the catalyst

$\text{H}_3\text{PW}_{12}\text{O}_{40}/\text{TiO}_2$ -3D_{spo-2}-12.7 and $\text{H}_3\text{PW}_{12}\text{O}_{40}/\text{TiO}_2$ -2D_{hex}-32.3 were chosen to evaluate the recyclability of the catalyst. The above DEP degradation reaction was repeated for five times. After the first catalytic run, the catalyst was removed by centrifugation and filtration, and then it was washed by hot water and dried at 120 °C. The recovered catalyst was used for subsequent catalytic runs under the same experimental conditions and regeneration method. It shows that the tested catalysts exhibit considerably high catalytic stability, and they can maintain a similar level of reactivity after five catalytic cycles (Fig. 10). To confirm the absence of $\text{H}_3\text{PW}_{12}\text{O}_{40}$ leaching into the reaction medium during the catalytic courses, the catalyst-free reaction solutions were

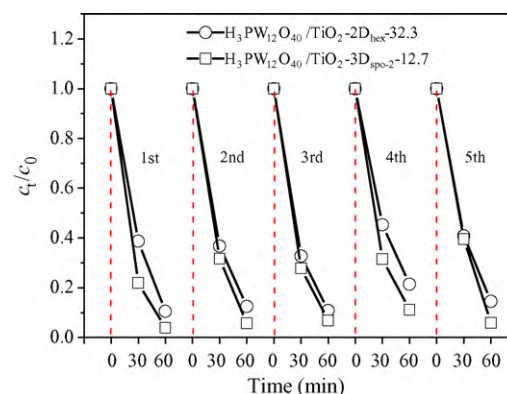


Fig. 10. Recyclability of mesoporous $\text{H}_3\text{PW}_{12}\text{O}_{40}/\text{TiO}_2$ materials for the photocatalytic degradation of an aqueous DEP. Simulated sunlight irradiation with $\lambda > 320$ nm, initial concentration of DEP 13.5 mg L⁻¹, volume 100 mL, catalyst amount 150 mg.

analyzed by ICP-AES to estimate the drop of $\text{H}_3\text{PW}_{12}\text{O}_{40}$. As expected, drop of $\text{H}_3\text{PW}_{12}\text{O}_{40}$ into the catalyst-free reaction solutions is lower than 0.01%. This high catalytic stability of the $\text{H}_3\text{PW}_{12}\text{O}_{40}/\text{TiO}_2$ materials is originated from the strong chemical interaction between the Keggin unit and TiO_2 matrix.

3.3.4. Discussion

The above photocatalytic tests indicate that the photocatalytic activity of as-prepared $\text{H}_3\text{PW}_{12}\text{O}_{40}/\text{TiO}_2$ materials is dominated by the following crucial factors.

Firstly, the incorporation of the Keggin unit with suitable loading within anatase TiO_2 support can result in the enhanced quantum efficiency, which is contributed by the strong electron accepting ability of the Keggin unit and surface defects of anatase TiO_2 lattices. On the one hand, the synergistic photocatalytic effect between the Keggin unit and TiO_2 matrix results in the retardation of the recombination of $\text{h}^+ - \text{e}^-$ pairs owing to trapping photogenerated electrons into unoccupied W5d states of the Keggin unit [45–47]. On the other hand, surface defects of anatase TiO_2 lattices are beneficial to photocatalytic activity because of reducing $\text{h}^+ - \text{e}^-$ recombination probability [48]. Surface defects can not only prolong the charge lifetime by trapping the charge carriers with defects but also transfer the trapped charges to the reactants. For the $\text{H}_3\text{PW}_{12}\text{O}_{40}/\text{TiO}_2\text{-}2\text{D}_{\text{hex}}$ materials with $\text{H}_3\text{PW}_{12}\text{O}_{40}$ loading from 8.8% to 41.2%, $\text{H}_3\text{PW}_{12}\text{O}_{40}/\text{TiO}_2\text{-}2\text{D}_{\text{hex}}\text{-}32.3$ and $\text{H}_3\text{PW}_{12}\text{O}_{40}/\text{TiO}_2\text{-}2\text{D}_{\text{hex}}\text{-}41.2$ showed the most obvious surface defects (Fig. 7), therefore, they showed comparably high photocatalytic activity towards DEP degradation under UV-light irradiation. Slightly lower activity of the $\text{H}_3\text{PW}_{12}\text{O}_{40}/\text{TiO}_2\text{-}2\text{D}_{\text{hex}}\text{-}41.2$ than the $\text{H}_3\text{PW}_{12}\text{O}_{40}/\text{TiO}_2\text{-}2\text{D}_{\text{hex}}\text{-}32.3$ is due to the fact that too high $\text{H}_3\text{PW}_{12}\text{O}_{40}$ loading may enrich tungsten atoms on the catalyst surface and thereby creating new recombination centers with decreased photocatalytic activity.

Secondly, at similar $\text{H}_3\text{PW}_{12}\text{O}_{40}$ loading, mesostructural orderings and pore geometries also play important roles to the photocatalytic activity of the $\text{H}_3\text{PW}_{12}\text{O}_{40}/\text{TiO}_2$ materials. For 3D disordered $\text{H}_3\text{PW}_{12}\text{O}_{40}/\text{TiO}_2$ materials, their higher catalytic activity than 3D ordered $\text{H}_3\text{PW}_{12}\text{O}_{40}/\text{TiO}_2$ material is due to their higher porosity, larger pore diameter, and higher crystallinity. Higher porosity can increase population of the active sites and accessibility to the active sites, while larger pore diameter can ensure the DEP degradation reaction performed in the pores totally and thereby decreasing the mass transfer limit. All of these factors have positive influence on the photocatalytic activity of 3D disordered $\text{H}_3\text{PW}_{12}\text{O}_{40}/\text{TiO}_2$. Slightly higher photocatalytic activity of the $\text{H}_3\text{PW}_{12}\text{O}_{40}/\text{TiO}_2\text{-}3\text{D}_{\text{spo-}2}\text{-}12.7$ than that of the $\text{H}_3\text{PW}_{12}\text{O}_{40}/\text{TiO}_2\text{-}3\text{D}_{\text{spo-}1}\text{-}12.3$ is due to larger pore diameter of the former than the latter. As for ordered 3D and 2D mesoporous $\text{H}_3\text{PW}_{12}\text{O}_{40}/\text{TiO}_2$ materials, they exhibited same textural properties, and their activity difference is due to different pore dimensions. 3D pore dimension can improve catalytic reactivity by facilitating the accessibility to the active sites in the framework; meanwhile, it can allow more efficient transport of guest species throughout the three-dimensional catalyst particle, and the reaction would not be limited to the catalyst surface only.

Thirdly, the crystallinity of the $\text{H}_3\text{PW}_{12}\text{O}_{40}/\text{TiO}_2$ material may be increased somewhat with increase the calcination temperature from 350 °C to 450 °C, but BET surface area decreased from 255 $\text{m}^2 \text{g}^{-1}$ to 199 $\text{m}^2 \text{g}^{-1}$ (for $\text{H}_3\text{PW}_{12}\text{O}_{40}/\text{TiO}_2\text{-}2\text{D}_{\text{hex}}\text{-}32.3$, see Table 1), meanwhile, the Keggin structure begin to decompose. These two factors lead to the decreased photocatalytic activity of $\text{H}_3\text{PW}_{12}\text{O}_{40}/\text{TiO}_2\text{-}2\text{D}_{\text{hex}}\text{-}32.3$ with increase the catalyst calcination temperature.

Finally, the band gap of the $\text{H}_3\text{PW}_{12}\text{O}_{40}/\text{TiO}_2$ materials is narrowed slightly compared with pure TiO_2 , which also has a positive effect to increase the photocatalytic activity of pure TiO_2 .

4. Conclusions

Mesostructured $\text{H}_3\text{PW}_{12}\text{O}_{40}$ -titania materials with controllable structural orderings and pore geometries were successfully obtained by designing the different preparation routes. As-prepared materials with suitable $\text{H}_3\text{PW}_{12}\text{O}_{40}$ loadings exhibited considerably higher photocatalytic activity to diethyl phthalate degradation with respect to pure TiO_2 under solar simulating Xe lamp irradiation (in the near UV- as well as visible-light region), attributed to the enhanced quantum efficiency contributed from the synergistic photocatalytic effect between the Keggin unit and titania matrix as well as the surface defects of the materials. Additionally, mesostructural orderings and pore geometries significantly influenced the photocatalytic activity of the $\text{H}_3\text{PW}_{12}\text{O}_{40}/\text{TiO}_2$ materials. Through suitable regeneration method, the materials can ensure little leakage of the Keggin unit and maintain similar level of activity after five catalytic cycles, performing as genuine heterogeneous photocatalysts to decompose aqueous organic pollutants effectively. This high catalytic stability of the $\text{H}_3\text{PW}_{12}\text{O}_{40}/\text{TiO}_2$ materials is originated from the strong chemical interaction between the Keggin unit and TiO_2 matrix.

Acknowledgements

This work is supported by the Key Project of Chinese Ministry of Education (308008); the Fundamental Research Funds for the Central Universities (09QNTD004); Natural Science Fund Council of China (20873018; 50878041); the Program of Changjiang Scholars and Innovative Research Team in University; and the Analysis and Testing Foundation of Northeast Normal University.

References

- [1] T.L. Thompson, J.T. Yates, Chem. Rev. 106 (2006) 4428–4453.
- [2] K.L. Lv, Y.M. Xu, J. Phys. Chem. B 110 (2006) 6204–6212.
- [3] I.P. Parkin, R.G. Palgrave, J. Mater. Chem. 15 (2005) 1689–1695.
- [4] X. Chen, S.S. Mao, Chem. Rev. 107 (2007) 2891–2959.
- [5] S. Wang, W. Hou, L. Wei, H. Jia, X. Liu, B. Xu, Surf. Coat. Technol. 202 (2007) 460–465.
- [6] J. Li, J. Xu, W. Dai, H. Li, K. Fan, Appl. Catal. B: Environ. 82 (2008) 233–243.
- [7] V. Puddu, R. Mokaya, G.L. Puma, Chem. Commun. 45 (2007) 4749–4751.
- [8] G. Marci, L. Palmisano, A. Sclafani, A.M. Venezia, R. Campostrini, G. Carturan, C. Martin, V. Rives, G. Solana, J. Chem. Soc., Faraday Trans. 92 (1996) 819–829.
- [9] H. Shibata, T. Ogura, T. Mukai, T. Ohkubo, H. Sakai, M. Abe, J. Am. Chem. Soc. 127 (2005) 16396–16397.
- [10] K. Fukuda, Y. Ebina, T. Shibata, T. Aizawa, I. Nakai, T. Sasaki, J. Am. Chem. Soc. 129 (2007) 202–209.
- [11] H. Li, Z. Bian, J. Zhu, Y. Huo, H. Li, Y. Lu, J. Am. Chem. Soc. 129 (2007) 4538–4539.
- [12] J.C. Yu, G. Li, X. Wang, X. Hu, C.W. Leung, Z. Zhang, Chem. Commun. (2006) 2717–2719.
- [13] D. Mitoraj, H. Kisch, Angew. Chem. Int. Ed. 47 (2008) 9975–9978.
- [14] G. Wu, J. Wang, D.F. Thomas, A. Chen, Langmuir 24 (2008) 3503–3509.
- [15] G. Liu, L. Wang, H. Yang, H. Cheng, G. Lu, J. Mater. Chem. 20 (2010) 831–843.
- [16] X. Yang, Y. Wang, L. Xu, X. Yu, Y. Guo, J. Phys. Chem. C 112 (2008) 11481–11489.
- [17] X. Yang, F. Ma, K. Li, Y. Guo, J. Hu, W. Li, M. Huo, Y. Guo, J. Hazard. Mater. 175 (2010) 429–438.
- [18] W. Schmidt, ChemCatChem 1 (2009) 53–67.
- [19] J.H. Clark, D.J. Macquarrie, S.J. Tavener, Dalton Trans. (2006) 4297–4309.
- [20] A. Taguchi, F. Schüth, Micropor. Mesopor. Mater. 77 (2005) 1–45.
- [21] F. Goettmann, C. Sanchez, J. Mater. Chem. 17 (2007) 24–30.
- [22] Y. Wan, D. Zhao, Chem. Rev. 107 (2007) 2821–2860.
- [23] K. Li, J. Hu, W. Li, F. Ma, L. Xu, Y. Guo, J. Mater. Chem. 19 (2009) 8628–8638.
- [24] I.V. Kozhevnikov, Chem. Rev. 98 (1998) 171–198.
- [25] N. Mizuno, M. Misono, Chem. Rev. 98 (1998) 199–217.
- [26] I.V. Kozhevnikov, J. Mol. Catal. A: Chem. 262 (2007) 86–92.
- [27] M. Misono, Chem. Commun. 13 (2001) 1141–1152.
- [28] Y. Guo, C. Hu, J. Cluster Sci. 14 (2003) 505–526.
- [29] Y. Guo, C. Hu, J. Mol. Catal. A: Chem. 262 (2007) 136–148.
- [30] T. Tachikawa, M. Fujitsuka, T. Majima, J. Phys. Chem. C 111 (2007) 5259–5275.
- [31] M. Yoon, J.A. Chang, Y. Kim, J.R. Choi, K. Kim, S.J. Lee, J. Phys. Chem. B 105 (2001) 2539–2545.
- [32] Y. Yang, Q. Wu, Y. Guo, C. Hu, E. Wang, J. Mol. Catal. A: Chem. 225 (2005) 203–212.
- [33] L. Li, Q. Wu, Y. Guo, C. Hu, Micropor. Mesopor. Mater. 87 (2005) 1–9.
- [34] G. Marci, E. García-López, L. Palmisano, D. Carriazo, C. Martín, V. Rives, Appl. Catal. B: Environ. 90 (2009) 497–506.

- [35] Y. Xie, L. Zhou, H. Huang, *Appl. Catal. B: Environ.* 76 (2007) 15–23.
- [36] S. Yanagida, A. Nakajima, T. Sasaki, T. Isobe, Y. Kameshima, K. Okada, *Appl. Catal. A: Gen.* 366 (2009) 148–153.
- [37] D. Carriazo, M. Addamo, G. Marci, C. Martín, L. Palmisano, V. Rives, *Appl. Catal. A: Gen.* 356 (2009) 172–179.
- [38] T.J. Wams, *Sci. Total Environ.* 66 (1987) 1–16.
- [39] B. Liu, H.C. Zeng, *Chem. Mater.* 20 (2008) 2711–2718.
- [40] W.J.J. Stevens, K. Lebeau, M. Mertens, G.V. Tendeloo, P. Cool, E.F. Vansant, *J. Phys. Chem. B* 110 (2006) 9183–9187.
- [41] L. Miao, S. Tanemura, S. Toh, K. Kaneko, M. Tanemura, *J. Cryst. Growth* 264 (2004) 246–252.
- [42] K. Li, Y. Guo, F. Ma, H. Li, L. Chen, Y. Guo, *Catal. Commun.* 11 (2010) 839–843.
- [43] L. Xu, Y. Wang, X. Yang, X. Yu, Y. Guo, J.H. Clark, *Green Chem.* 10 (2008) 746–755.
- [44] P.M. Rao, A. Wolfson, S. Kababya, S. Vega, M.V. Landau, *J. Catal.* 232 (2005) 210–225.
- [45] P. Kormali, T. Triantis, D. Dimotikali, A. Hiskia, E. Papaconstantinou, *Appl. Catal. B: Environ.* 68 (2006) 139–146.
- [46] C. Chen, P. Lei, H. Ji, W. Ma, J. Zhao, H. Hidaka, N. Serpone, *Environ. Sci. Technol.* 38 (2004) 329–337.
- [47] T. Tachikawa, M. Fujitsuka, T. Majima, *J. Phys. Chem. C* 111 (2007) 5259–5275.
- [48] S. Chang, C. Hou, P. Lo, C. Chang, *Appl. Catal. B: Environ.* 90 (2009) 233–241.